Atom-Interferometric Test of the Equivalence Principle at the 10^{-12} Level

Peter Asenbaum,* Chris Overstreet,* Minjeong Kim, Joseph Curti, and Mark A. Kasevich†
Department of Physics, Stanford University, Stanford, California 94305, USA

(Received 26 June 2020; accepted 5 October 2020; published 2 November 2020)

We use a dual-species atom interferometer with 2 s of free-fall time to measure the relative acceleration between ^{85}Rb and ^{87}Rb wave packets in the Earth's gravitational field. Systematic errors arising from kinematic differences between the isotopes are suppressed by calibrating the angles and frequencies of the interferometry beams. We find an Eötvös parameter of $\eta = [1.6 \pm 1.8(\text{stat}) \pm 3.4(\text{syst})] \times 10^{-12}$, consistent with zero violation of the equivalence principle. With a resolution of up to 1.4×10^{-11} g per shot, we demonstrate a sensitivity to η of $5.4 \times 10^{-11}/\sqrt{\text{Hz}}$.

DOI: 10.1103/PhysRevLett.125.191101

Does gravity influence local measurements? The equivalence principle (EP), which posits that all gravitational effects disappear locally [1], is the foundation of general relativity [2] and other geometric theories of gravity. Most theoretical unification attempts that couple gravity to the standard model lead to EP violations [3]. In addition, tests of the equivalence principle search for perturbations of geometric gravity and are sensitive to exotic interactions [4,5] that couple differently to the test masses. These tests are complementary to searches for large-scale variations of unknown fields [6] and are carried out with local probes that can be precisely controlled.

EP tests are often characterized by the Eötvös parameter η, which is the relative acceleration of the test masses divided by the average acceleration between the test masses and the nearby gravitational source. With classical accelerometers, EP violation has been constrained to $\eta < 1.8 \times 10^{-13}$ by torsion balances in a laboratory setting [7] and to $\eta < 1.3 \times 10^{-14}$ by the concluded space mission *MICROSCOPE* [8].

We perform an equivalence principle test by interferometrically measuring the relative acceleration of freely falling clouds of atoms. Atom clouds are well-suited test masses because they spend 99.9% of the interrogation time in free fall and the remainder in precisely controlled interactions with the interferometry lasers. In addition, atoms have uniform and well-characterized physical properties. Compared to classical tests, atom-interferometric (AI) EP tests are influenced by different sources of systematic error [9]. AI EP tests can be performed between isotopes that differ only in neutron number, and quantum tests are especially sensitive to particular violation mechanisms [10]. However, previous AI EP tests [11–14] have been limited to $\eta < 3 \times 10^{-8}$ in dual-species comparisons [14] and $\eta < 1.4 \times 10^{-9}$ in comparisons between ground states of a single species [15], largely due to a lack of sensitivity compared to classical experiments.

In this Letter, we report an atom-interferometric test of the equivalence principle between ^{85}Rb and ^{87}Rb with $\eta = [1.6 \pm 1.8(\text{stat}) \pm 3.4(\text{syst})] \times 10^{-12}$, consistent with zero violation at the 10^{-12} level. This result improves by four orders of magnitude on the best previous dual-species EP test with atoms [14]. We achieve high sensitivity by utilizing a long interferometer time T and a large momentum splitting between interferometer arms. With a resolution of 1.4×10^{-11} g per shot and 15 s cycle time, the interferometer attains the highest sensitivity to η of any laboratory experiment to date [7].

The relative acceleration between ^{85}Rb and ^{87}Rb is measured with a dual-species atom interferometer. The experimental apparatus is described in [16]. We prepare ultracold clouds of ^{85}Rb and ^{87}Rb by evaporative cooling in a magnetic trap. The subsequent magnetic lensing sequence lowers the horizontal kinetic energies to 25 nK but introduces a 1.8 mm vertical offset between the two isotopes. The other kinematic degrees of freedom (d.o.f.) remain matched. The clouds are then trapped in a vertical 1D optical lattice and accelerated to 13 m/s in 20 ms (launch height ~8.6 m). This laser lattice launch accelerates the atoms to approximately the final lattice velocity. Each isotope is accelerated to a distinct, even multiple of its recoil velocity $\hbar k/m$. We choose a final lattice velocity such that the vertical velocities of the two isotopes are overlapped to within 1 mm/s. To spatially overlap the clouds, we apply species-selective Raman transitions that kick the two isotopes in opposite directions. After a 77 ms drift time and removal of untransferred atoms, the Raman transitions are reversed, and the clouds are overlapped to within 65 μm. The Raman pulses also provide velocity selection, and the detunings of the Raman pulses allow the average vertical velocity of each isotope to be individually controlled, improving the velocity overlap to within 60 μm/s.

The interferometer beam splitters consist of sequences of two-photon Bragg transitions [16] that transfer $4\hbar k$, $8\hbar k$, or

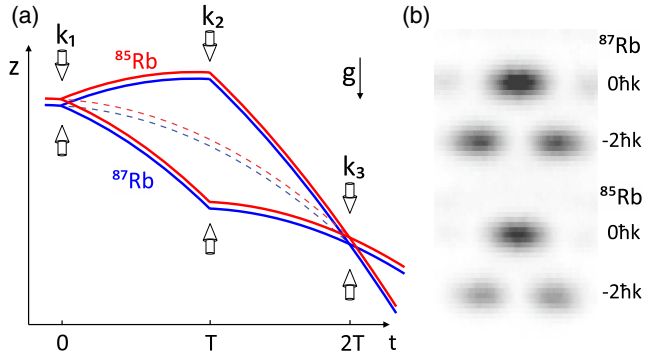

FIG. 1. (a) Schematic of simultaneous ^{85}Rb and ^{87}Rb interferometer in the initial rest frame of the atoms (not to scale). In pulse zone 1 ($t = 0$), each atom cloud is split into two interferometer paths with $\hbar\mathbf{k}_1$ momentum difference. In pulse zone 2 ($t = T$), the paths are reflected toward each other with wave vector $\mathbf{k}_2$. In pulse zone 3 ($t = 2T$), the paths are recombined and interfered with wave vector $\mathbf{k}_3$. The effective wave vectors $\mathbf{k}_1$, $\mathbf{k}_2$, and $\mathbf{k}_3$ differ slightly in orientation and magnitude to create a tailored phase response to kinematic initial conditions. The midpoint trajectory of each isotope remains essentially unperturbed throughout the interferometer; the ^{85}Rb and ^{87}Rb midpoint trajectories are overlapped to within 65 μm. (b) Single fluorescence image (14.8 mm × 25.6 mm) of ^{85}Rb and ^{87}Rb output ports ($0\hbar k$ and $-2\hbar k$) with $8\hbar k$ beam splitters. The detection fringe allows precise single-shot phase extraction.

$12\hbar k$ momentum. The pulses addressing each interferometer arm are interleaved, and the time interval between successive transitions is 3 ms. Collectively, these pulses split the clouds symmetrically in the vertical direction. The symmetric interferometer geometry guarantees that the midpoint trajectory [17] of each isotope remains essentially unperturbed. The interferometer duration $2T$ is 1910 ms, and the maximum wave packet separation for $12\hbar k$ is 6.9 cm (6.7 cm) for ^{85}Rb (^{87}Rb). After a total drift time of 2.5 s, the output ports (separated by $2\hbar k$ momentum [18]) are imaged with two orthogonal CCD cameras along the horizontal directions. One isotope is imaged with a time delay of 1 ms so that the two species can be individually resolved. The phase of each interferometer is given by the population ratio of its output ports. Figure 1(a) shows a schematic of the interferometer sequence.

In an EP test configuration, the differential phase between ^{85}Rb and ^{87}Rb is close to zero. To distinguish small positive from small negative differential phases, a precise phase offset is needed. By adjusting the angles of the interferometry beams, we imprint a horizontal phase gradient so that each image contains a full interference fringe. This "detection fringe" is highly common to both isotopes and allows the contrast and phase of each interferometer to be extracted from a single shot; see Supplemental Material for additional details [19]. Figure 1(b) shows a fluorescence image in which the detection fringe is visible.

The differential phase shift $\Delta\phi = nk\Delta g T^2$ is proportional to the relative acceleration Δg between the atoms. We achieve a single-shot differential phase resolution of up to 8 mrad in an $8\hbar k$ interferometer, determined from the observed standard deviation of the differential phase in a set of 20 shots. This resolution corresponds to a relative acceleration sensitivity of 1.4×10^{-11} g per shot with duty cycle 15 s. The observed noise is close to the atomic shot noise limit with $\sim 10^5$ atoms per interferometer and interference contrast of 70%. In each data run, the initial beam splitter direction, number of photon recoils n per beam splitter (4, 8, or 12), detection fringe direction, and imaging order are permuted. The differential phase is averaged over initial beam splitter direction, detection fringe direction, and imaging order to suppress systematic errors. A full run consists of about 20 shots in each configuration (480 shots total). The statistical sensitivity is derived from three full runs taken on three separate days. Throughout the data-taking and analysis process, the EP result was blinded by the addition of an unknown offset to each differential phase measurement.

Systematic errors arise from effects that shift the ^{85}Rb interferometer phase relative to the ^{87}Rb phase. In our experiment, there are three significant sources of systematic error: differences in kinematic d.o.f., differences in the interaction with the electromagnetic field, and imaging errors. A summary of the systematic errors is presented in Table I. The most significant systematic effects are described in the text below, and additional errors are discussed in the Supplemental Material [19]. The final

TABLE I. Error budget in units of 10^{-12} g. The parameter Δz (Δv_z) includes all errors that are linearly proportional to the initial vertical position (velocity) difference between the two isotopes. Likewise, Δx (Δv_x) includes all errors proportional to the initial position (velocity) difference in the detection fringe direction, and Δy (Δv_y) includes all errors proportional to the initial position (velocity) difference in the orthogonal horizontal direction. See main text and Supplemental Material [19] for descriptions of other systematic errors. All uncertainties are 1σ. For entries in which no shift value is recorded, the shift is zero.

Parameter	Shift	Uncertainty
Total kinematic	1.5	2.0
Δz		1.0
Δv_z	1.5	0.7
Δx		0.04
Δv_x		0.04
Δy		0.2
Δv_y		0.2
Width		1.6
ac-Stark shift		2.7
Magnetic gradient	−5.9	0.5
Pulse timing		0.04
Blackbody radiation		0.01
Total systematic	−4.4	3.4
Statistical		1.8

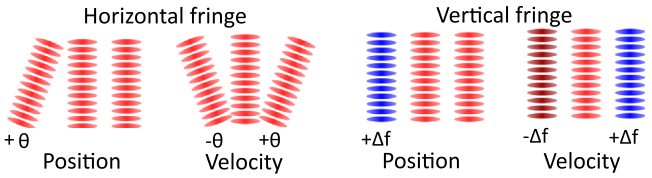

FIG. 2. Compensation method for kinematic d.o.f. Changing the angle (frequency) of pulse zone 1 creates a horizontal (vertical) position-dependent phase. Changing the angle (frequency) of pulse zone 1 by $-\theta$ ($-\Delta f$) and pulse zone 3 by θ (Δf) creates a horizontal (vertical) velocity-dependent phase. The angle and frequency steps are calibrated to eliminate phase sensitivity to kinematic d.o.f.

result of the Eötvös parameter is the sum of the total systematic shift and the mean of the differential acceleration measurements.

The relevant kinematic d.o.f. are the initial position and velocity of each species in the vertical and horizontal directions. Each species is coupled by its kinematic d.o.f. to the gravity gradient and to the wave front of the interferometry beams. In order to reduce the associated systematic errors, we minimize differences in the kinematic d.o.f. and also suppress the sensitivity of the interferometer to them. The phase sensitivity to the vertical d.o.f. can be minimized by adjusting the frequency of the interferometry lasers between each pulse zone, and the phase sensitivity to the horizontal d.o.f. can be minimized by adjusting the angles of the lasers (Fig. 2).

To be concrete, suppose that the average frequency of the interferometry lasers during pulse zone 2 is f. Changing the average frequency of pulse zone 1 to $f + \Delta f_1$ adds a phase shift $2\pi/cn\Delta f_1 z$, where n is the number of photon recoils and z is the initial vertical position. Similarly, if the average frequency of pulse zone 3 is $f + \Delta f_3$, the added phase shift $2\pi/cn\Delta f_3(z + 2v_z T)$ depends on the initial vertical velocity v_z. Gravity gradients cause systematic errors that are proportional to the vertical initial conditions [16,23]. By choosing the appropriate combination of Δf_1 and Δf_3, we can simultaneously minimize the phase sensitivity to z and v_z, realizing a generalized version of the compensation technique reported in [16,24]. To calibrate the pulse zone frequencies, we vertically displace the two isotopes in each d.o.f. and choose Δf_1 and Δf_3 to minimize the dependence of the differential phase on the displacement (see Supplemental Material for details [19]).

An analogous technique can be used to suppress the sensitivity of the interferometer to horizontal d.o.f. Suppose that the beam angle during pulse zone 2 is $\theta_2 = 0$. Setting the angle of pulse zone 1 to θ_1 in the xz plane adds the phase shift $nk\theta_1 x$, where x is the initial horizontal position. Likewise, the angle θ_3 in pulse zone 3 adds the phase shift $nk\theta_3(x + 2v_x T)$, where v_x is the initial horizontal velocity. An appropriate choice of angles in each horizontal direction provides complete compensation of linear phase gradients from the interferometer wave front. Such phase gradients arise due to the rotation of the Earth [25].

We control the angle of the interferometry lasers in each pulse zone by setting the angle of the mirror that retroreflects them. This angle is adjusted during the interferometer to undo the velocity-dependent phase that would otherwise be imprinted by the Earth's rotation. To calibrate the rotation rate, we add and subtract an additional velocity-dependent phase in a ^{87}Rb interferometer and null the fringe frequency difference [25]. This procedure suppresses phase shifts proportional to horizontal velocity by a factor of 1000. For the EP test, we imprint a horizontal phase that is proportional to the detected position (a combination of initial position and initial velocity; see Supplemental Material [19] for additional information). The use of a detection fringe for phase readout avoids systematic errors from initial horizontal displacements between the isotopes.

These compensation techniques allow us to suppress all phase shifts that arise from linear horizontal or vertical phase gradients. However, the atom clouds also have a finite width that can couple to higher-order horizontal wave front perturbations. To bound this effect, we correlate the cloud width with the differential phase and measure the phase difference between the middle and the edge of each cloud.

To extract the relative acceleration between ^{85}Rb and ^{87}Rb, we compare the differential phase of interferometers with beam splitter momentum $n\hbar k$, where $n \in \{4, 8, 12\}$ (Fig. 3). The relative acceleration is given by the linear dependence of the differential phase on n. We vary n by adding additional $2\hbar k$ pulses to each pulse zone. This approach eliminates systematic errors that arise from the finite duration and detuning of the initial and final $\pi/2$ beam splitter pulses [26,27], which are the same for all n.

The direction of the initial and final beam splitters, set by the frequency difference between interferometry beams, determines the momenta of the interferometer output ports (either $\{2\hbar k, 0\hbar k\}$ or $\{0\hbar k, -2\hbar k\}$ with respect to the

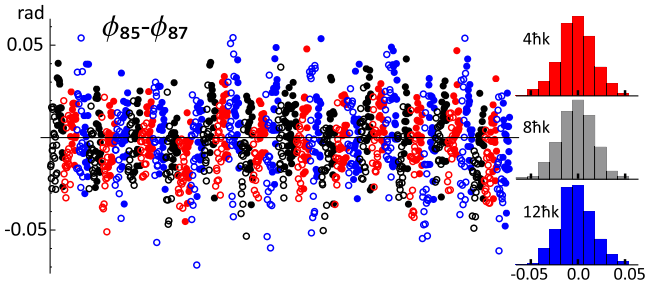

FIG. 3. EP data (1481 shots). Left: time series of the interferometer phase difference $\phi_{85} - \phi_{87}$, color coded by interferometer order ($4\hbar k$ red, $8\hbar k$ gray, $12\hbar k$ blue). Hollow (solid) points represent measurements with initial beam splitter direction down (up). Right: Histogram of the phase difference as a function of interferometer order, averaged over beam splitter direction, detection fringe direction, and imaging order.

launched clouds). We switch the beam splitter direction to identify phase shifts that scale with k^2. Such phase shifts arise due to parasitic recoil interferometers [28] that are caused by imperfect transfer efficiency. The phase of a recoil-sensitive interferometer scales as $\hbar k^2 T/m$, and the dependence on the mass m creates a systematic error in the EP measurement. When the beam splitter direction is reversed, the recoil phase shifts change sign relative to the acceleration-induced phase shift, allowing the two effects to be distinguished.

Electromagnetic interactions cause significant systematic errors in two ways. First, a differential acceleration arises from off-resonant forces (ac-Stark shifts) induced by the interferometry lasers. This effect is reduced by using an optical spectrum that suppresses the shifts of the ^{87}Rb $F = 2$ and ^{85}Rb $F = 3$ states. To lowest order in the wave packet separation, the differential Stark shift $\Delta\phi_S$ in our interferometer geometry is given by $\Delta\phi_S = (f_{85}/m_{85} - f_{87}/m_{87})2\pi(n-1)\beta(n\hbar k T)$, where β is the fractional intensity gradient at the height of the middle pulse zone and f_i is a factor that characterizes the Stark shift suppression of isotope i. The interferometry beams have a $1/e^2$ radius of 2 cm and are retroreflected at an angle of 0.5 mrad to avoid étaloning, which creates a fractional intensity gradient $\beta = 1 \times 10^{-3}/(5\text{ cm})$. Reducing the differential Stark shift to $\sim$1 mrad in a $12\hbar k$ interferometer requires $f_i \sim 10^{-2}$.

Our optical spectrum is designed to achieve $f_i \sim 10^{-2}$ for both isotopes simultaneously. The 780 nm spectrum of each interferometry beam is created by frequency doubling a 1560 nm laser that is phase modulated at 30 GHz. After doubling, the spectrum consists of two strong sidebands and a highly suppressed carrier with relative intensity $\sim 10^{-3}$. The carrier frequency is positioned between the ^{85}Rb $F = 3 \rightarrow F'$ transitions and the ^{87}Rb $F = 2 \rightarrow F'$ transitions, which are separated by 1 GHz. The blue-detuned sidebands are used to drive Bragg transitions, and the red-detuned sidebands compensate the optical forces from the blue-detuned sidebands [29]. To bound the magnitude of the residual ac-Stark effect, we add additional off-resonant pulses to an $8\hbar k$ interferometer (see Supplemental Material [19] for details). We observe no statistically significant differential phase shift with these additional pulses, which implies that residual ac-Stark effect induces a differential acceleration below 2.7×10^{-12} g.

Second, the two isotopes are differentially accelerated by magnetic forces. This effect is reduced by creating a nearly uniform magnetic field in the interferometry region via a solenoid coil and three layers of magnetic shielding [30]. The atoms enter the shielded region in the magnetically sensitive states $|F = 3, m_F = 3\rangle$ (^{85}Rb) and $|F = 2, m_F = 2\rangle$ (^{87}Rb). A series of microwave pulses transfers the atoms to the magnetically insensitive states $|F = 3, m_F = 0\rangle$ (^{85}Rb) and $|F = 2, m_F = 0\rangle$ (^{87}Rb). Nevertheless, the second-order Zeeman effect causes a phase shift $\phi_i = -2(\hbar/m_i)\alpha_i B(\partial_z B)kT^2$ of each isotope, where α_i is the second-order Zeeman coefficient of isotope i, B is the magnetic field magnitude, $\partial_z B$ is the vertical magnetic field gradient, and m_i is the mass of isotope i. To measure $\partial_z B$, we compare the phase of a ^{87}Rb interferometer in state $|F = 2, m_F = 1\rangle$ with the phase of a ^{87}Rb interferometer in state $|F = 2, m_F = 0\rangle$ (see Supplemental Material [19] for details). At $B = 41$ mG, the $|F = 2, m_F = 1\rangle$ interferometer has an increased sensitivity to magnetic field gradients by five orders of magnitude. The magnetic field gradient in the interferometry region averages to (-0.41 ± 0.036) mG/m, which corresponds to a differential acceleration of $(5.9 \pm 0.5) \times 10^{-12}$ g in the EP measurement.

The phase of each interferometer is encoded in the spatial position of the imaged detection fringe. Therefore, imaging differences between the isotopes can give rise to systematic errors. To image both species in a single CCD frame, the fluorescence light for one species is delayed by 1 ms, during which the two isotopes drift apart by 1 cm. The CCD axis is misaligned with respect to the drift direction by 4 mrad, which causes a differential phase shift of 40 mrad. To eliminate this phase shift, we rotate the camera images in software. We also switch the imaging order and reverse the direction in which the detection fringe is imprinted, each of which changes the sign of imaging-related phase shifts relative to the EP signal. The imaging order and detection fringe direction can each be reversed with fidelity > 0.99. Together, these reversals ensure that imaging effects do not contribute significantly to the systematic error.

We have tested the equivalence principle between ^{85}Rb and ^{87}Rb at the level of 10^{-12} g. The result is consistent with $\eta = 0$, which places generic constraints on new interactions that would differentially accelerate the two isotopes. The systematic uncertainty is primarily limited by the ac-Stark shift, which can be reduced with an improved laser system that operates at larger single-photon detuning. Such a system would also allow the momentum transfer in each pulse zone to be increased, improving the single-shot sensitivity and reducing the time required to characterize systematic errors. Uncertainties associated with linear kinematic errors can be reduced to arbitrarily small values by decreasing the statistical uncertainties in the calibration of the compensating frequencies and angles. The shift due to the magnetic gradient can be reduced by tailoring the current through each segment of the solenoid within the magnetic shield. By demonstrating that the high sensitivity of large-area atom interferometers can be utilized in precision measurement applications, this work provides a proof of concept for future AI EP tests in space [31] and gravitational wave detectors [32,33].

We acknowledge funding from the Defense Threat Reduction Agency, the Office of Naval Research, and

the Vannevar Bush Faculty Fellowship program. M. K. acknowledges funding from the Kwanjeong Educational Foundation. We thank Robin Corgier, Salvador Gomez, Jason Hogan, Tim Kovachy, Remy Notermans, and Stefan Seckmeyer for their assistance with this work.

*These authors contributed equally to this work.
†kasevich@stanford.edu

[1] W. Pauli, in *Encyklopädie der mathematischen Wissenschaften, mit Einschluss an ihrer Anwendung*, edited by A. Sommerfeld (Teubner, Leipzig, 1921), Vol. 5, pp. 539–775.
[2] S. Weinberg, *Gravitation and Cosmology: Principles and Applications of the General Theory of Relativity* (Wiley, New York, 1972).
[3] T. Damour, Classical Quantum Gravity **13**, A33 (1996).
[4] P. W. Graham, D. E. Kaplan, J. Mardon, S. Rajendran, and W. A. Terrano, Phys. Rev. D **93**, 075029 (2016).
[5] A. Hees, O. Minazzoli, E. Savalle, Y. V. Stadnik, and P. Wolf, Phys. Rev. D **98**, 064051 (2018).
[6] A. Arvanitaki, P. W. Graham, J. M. Hogan, S. Rajendran, and K. Van Tilburg, Phys. Rev. D **97**, 075020 (2018).
[7] S. Schlamminger, K.-Y. Choi, T. A. Wagner, J. H. Gundlach, and E. G. Adelberger, Phys. Rev. Lett. **100**, 041101 (2008).
[8] P. Touboul, G. Métris, M. Rodrigues, Y. André, Q. Baghi *et al.*, Phys. Rev. Lett. **119**, 231101 (2017).
[9] J. M. Hogan, D. M. S. Johnson, and M. A. Kasevich, in *Proceedings of the International Summer School of Physics "Enrico Fermi" on Atom Optics and Space Physics*, edited by E. Arimondo, W. Ertmer, and W. P. Schleich (IOS Press, Amsterdam, 2009), pp. 411–447.
[10] E. Göklü and C. Lämmerzahl, Classical Quantum Gravity **25**, 105012 (2008).
[11] A. Bonnin, N. Zahzam, Y. Bidel, and A. Bresson, Phys. Rev. A **88**, 043615 (2013).
[12] D. Schlippert, J. Hartwig, H. Albers, L. L. Richardson, C. Schubert, A. Roura, W. P. Schleich, W. Ertmer, and E. M. Rasel, Phys. Rev. Lett. **112**, 203002 (2014).
[13] M. G. Tarallo, T. Mazzoni, N. Poli, D. V. Sutyrin, X. Zhang, and G. M. Tino, Phys. Rev. Lett. **113**, 023005 (2014).
[14] L. Zhou *et al.*, Phys. Rev. Lett. **115**, 013004 (2015).
[15] G. Rosi, G. D'Amico, L. Cacciapuoti, F. Sorrentino, M. Prevedelli, M. Zych, Č. Brukner, and G. M. Tino, Nat. Commun. **8**, 15529 (2017).
[16] C. Overstreet, P. Asenbaum, T. Kovachy, R. Notermans, J. M. Hogan, and M. A. Kasevich, Phys. Rev. Lett. **120**, 183604 (2018).
[17] C. Antoine and C. J. Bordé, J. Opt. B **5**, S199 (2003).
[18] The output ports are separated by $2\hbar k$ momentum in every configuration because the final beam splitter pulse is always a two-photon transition.
[19] See Supplemental Material at http://link.aps.org/supplemental/10.1103/PhysRevLett.125.191101 for additional information on methods and systematic errors, which includes Refs. [20–22].
[20] M. Sonnleitner, M. Ritsch-Marte, and H. Ritsch, Phys. Rev. Lett. **111**, 023601 (2013).
[21] P. Haslinger, M. Jaffe, V. Xu, O. Schwartz, M. Sonnleitner, M. Ritsch-Marte, H. Ritsch, and H. Müller, Nat. Phys. **14**, 257 (2018).
[22] J. E. Debs, P. A. Altin, T. H. Barter, D. Döring, G. R. Dennis, G. McDonald, R. P. Anderson, J. D. Close, and N. P. Robins, Phys. Rev. A **84**, 033610 (2011).
[23] P. Asenbaum, C. Overstreet, T. Kovachy, D. D. Brown, J. M. Hogan, and M. A. Kasevich, Phys. Rev. Lett. **118**, 183602 (2017).
[24] A. Roura, Phys. Rev. Lett. **118**, 160401 (2017).
[25] A. Sugarbaker, S. M. Dickerson, J. M. Hogan, D. M. S. Johnson, and M. A. Kasevich, Phys. Rev. Lett. **111**, 113002 (2013).
[26] C. Antoine, Appl. Phys. B **84**, 585 (2006).
[27] C. J. Bordé and C. Lämmerzahl, Ann. Phys. (Paris) **8**, 83 (1999).
[28] P. A. Altin *et al.*, New J. Phys. **15**, 023009 (2013).
[29] T. Kovachy, P. Asenbaum, C. Overstreet, C. A. Donnelly, S. M. Dickerson, A. Sugarbaker, J. M. Hogan, and M. A. Kasevich, Nature (London) **528**, 530 (2015).
[30] S. Dickerson, J. M. Hogan, D. M. S. Johnson, T. Kovachy, A. Sugarbaker, S.-w. Chiow, and M. A. Kasevich, Rev. Sci. Instrum. **83**, 065108 (2012).
[31] D. Aguilera *et al.*, Classical Quantum Gravity **31**, 115010 (2014).
[32] B. Canuel *et al.*, Sci. Rep. **8**, 14064 (2018).
[33] J. Coleman, arXiv:1812.00482.